Supplementary material.
Supplemental Figure S1.

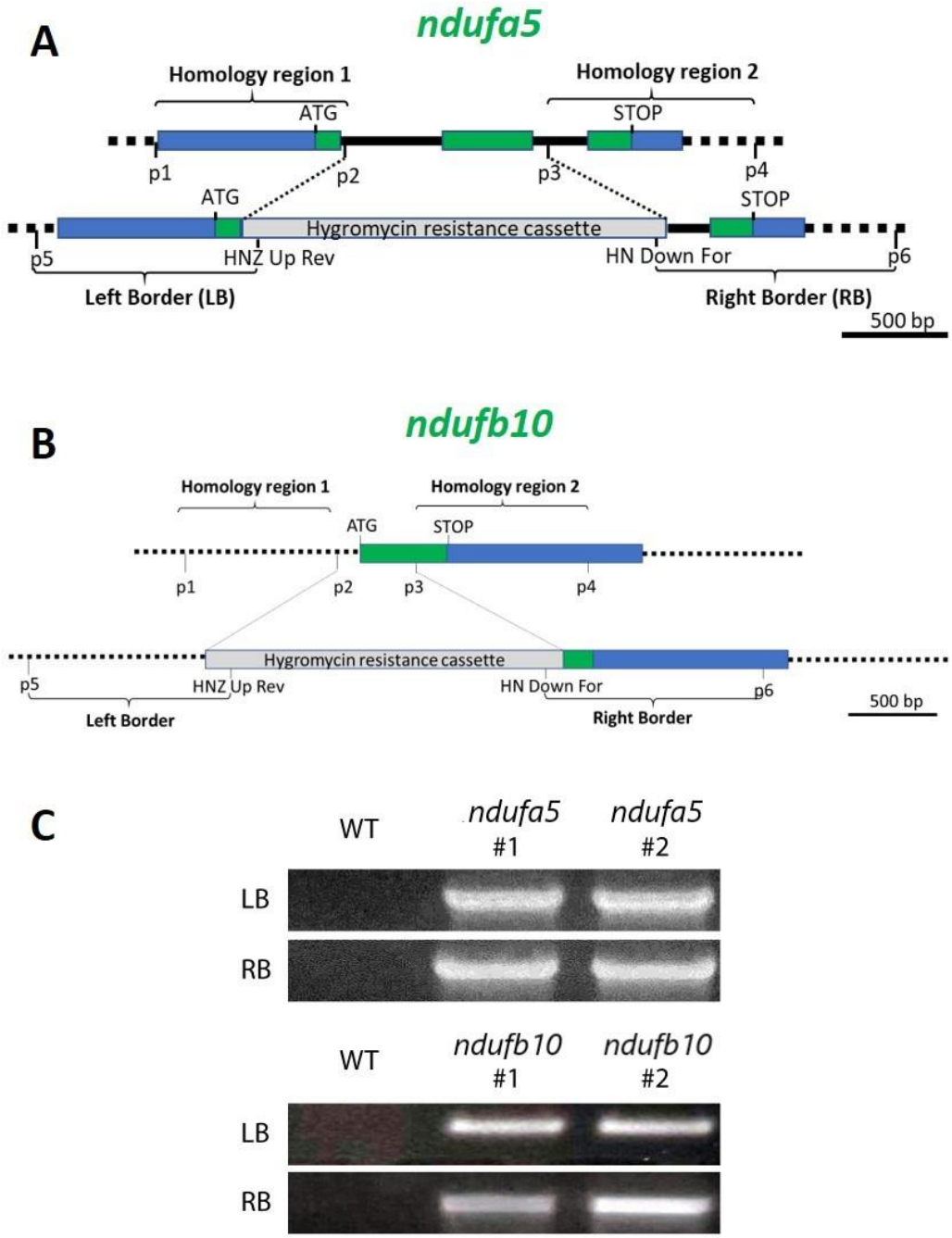

Supplemental Figure S1. Generation of *P. patens* mutant lines lacking respiratory complex I A-B) KO scheme for *Ndufa5* and *Ndufb10* respectively, showing the CDS, the regions of homology chosen to drive homologous recombination and insertion of the resistance cassette. In A and B are indicated the position of the primers employed for recombination cassette construction (p1, p2, p3 and p4) and primers employed in mutant screening (p5, p6, HNZ Up Rev and HN Down for). C) Example of PCR for verification of the homologous recombination event. PCR products (called Left and Right Border, LB and RB; all PCR products have an expected size of ca 1200 bp. LB was performed with primer p5 and HNZ Up rev while RB was performed with HN Down for and p6) are generated only if the resistance cassette is inserted in the expected genomic region.

Supplemental Figure S2.

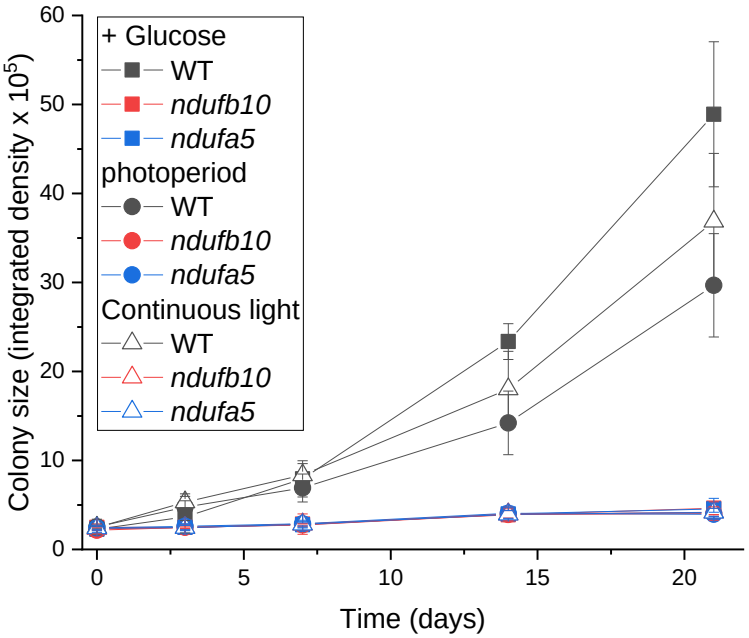

Supplemental Figure S2. Growth kinetics of *P. patens* plants under different conditions. Plants were grown under different light regimes and different medium composition as shown in Figure 2 and their size was evaluated after 0, 3, 7, 14 and 21 days of growth. All plants were exposed to 50 µmol photons m^{-2} s^{-1}. Squares show growth in medium supplemented with 0.5% of glucose, circles growth at 16h light/8h light/dark photoperiod in minimal medium, triangles growth under continuous light regime in minimal medium. WT, *ndufb10* and *ndufa5* KO are shown respectively in black, red and blue. Average ± SD ($n \geq 5$) is reported.

Supplemental Figure S3.

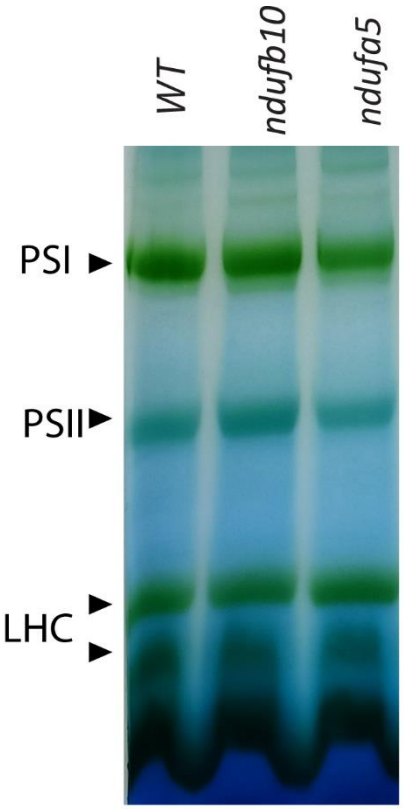

Supplemental Figure S3. BN-PAGE separation of crude extracts. Crude membrane protein extracts from WT, *ndufb10* and *ndufa5* were solubilized with 1% of β-dodecyl maltoside (β-DM). Complexes of thylakoid membranes identifiable as green bands are indicated; PSI, Photosystem I; PSII, photosystem II; LHC, light-harvesting chlorophyll complexes.

Supplemental Figure S4.

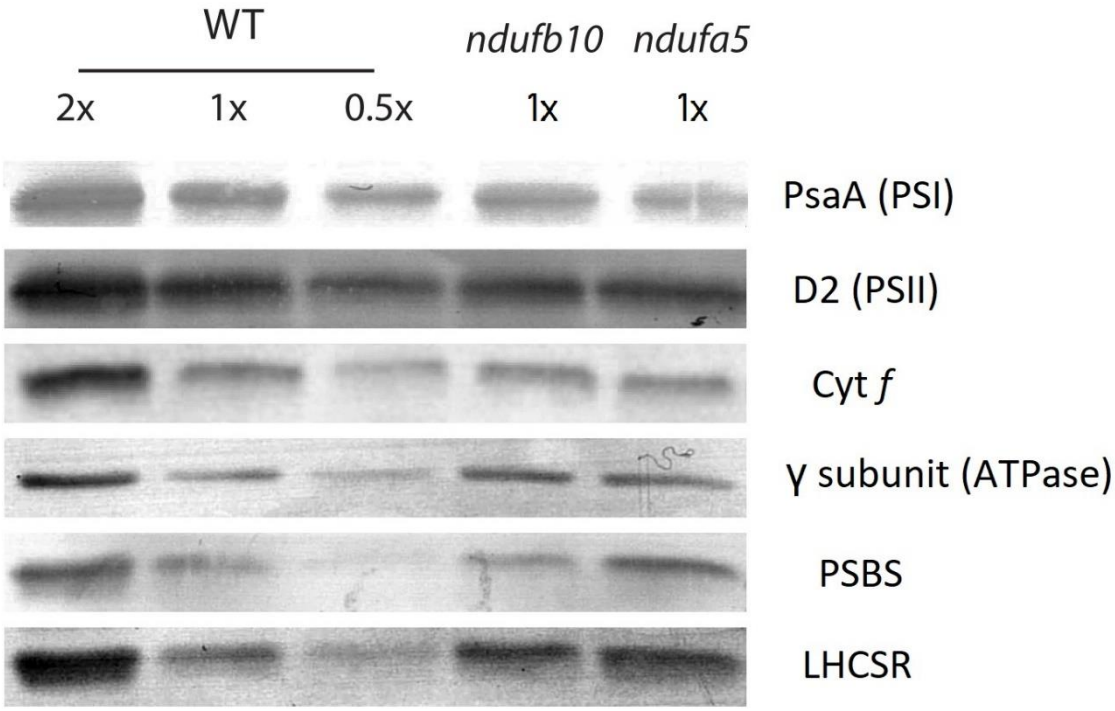

Supplemental Figure S4. Impact of Complex I mutations on the photosynthetic apparatus composition. Immunoblot analysis of various proteins of the photosynthetic apparatus. For WT 1X, *ndufb10* and *ndufa5* a total protein extract amount equivalent to 2 µg of total chlorophyll was loaded. 2X and 0.5X correspond to an equivalent of 4 µg and 1 µg of total chlorophyll. PSI and PSII, Photosystem I and II; Cyt, Cytochrome.

Supplemental Figure S5.

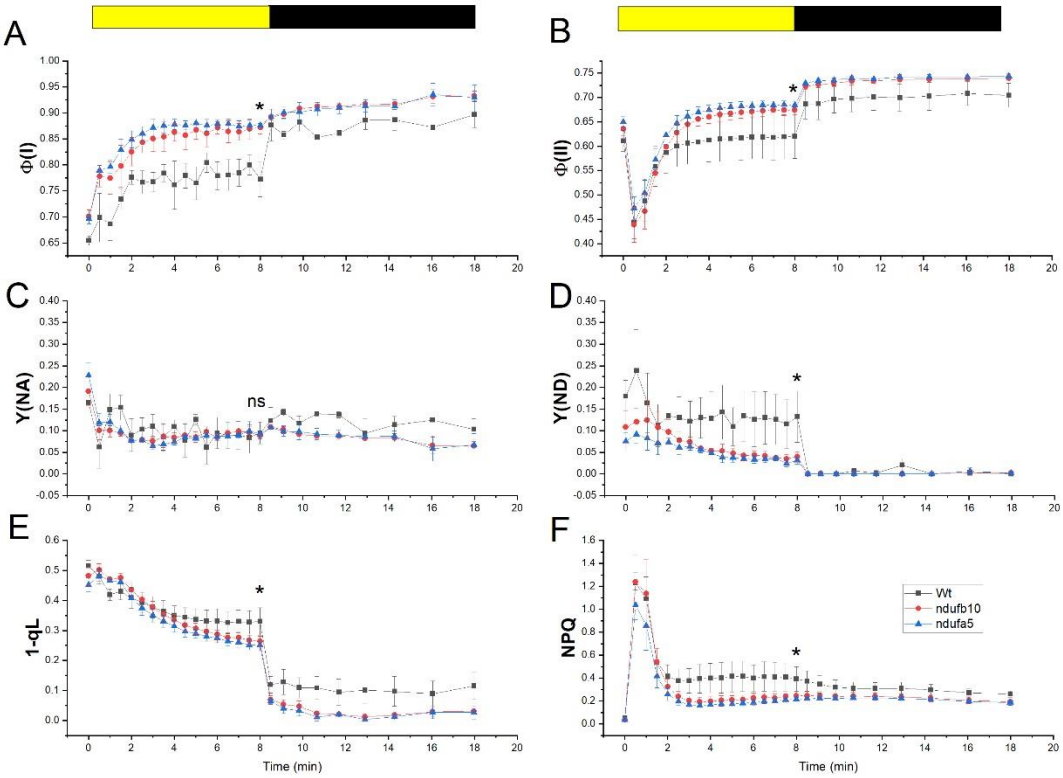

Supplemental Figure S5. Photosynthetic efficiency under dim illumination. The yield of PSI (Φ(I), A), PSII (Φ(II), B). PSI acceptor side limitation (Y(NA), C), PSI donor side limitation (Y(ND), D). PQ redox state (1-qL; E) and non-photochemical quenching (NPQ; F) were monitored under illumination of 50 µmol photons $m^{-2}s^{-1,}$ corresponding to light intensity during growth. WT, *ndufb10* and *ndufa5* KO are shown respectively as black squares, red circles and blue triangles. Yellow/black bar indicates light on/off. Data are shown as average ± SD ($n > 4$). Asterisks indicate statistically significant differences (one-way ANOVA, $n > 5$, $p < 0.01$) between WT and both mutants while ns indicates when eventual differences are not statically significant. Statistical analyses were performed for the last point before light was switched off.

Supplemental Figure S6.

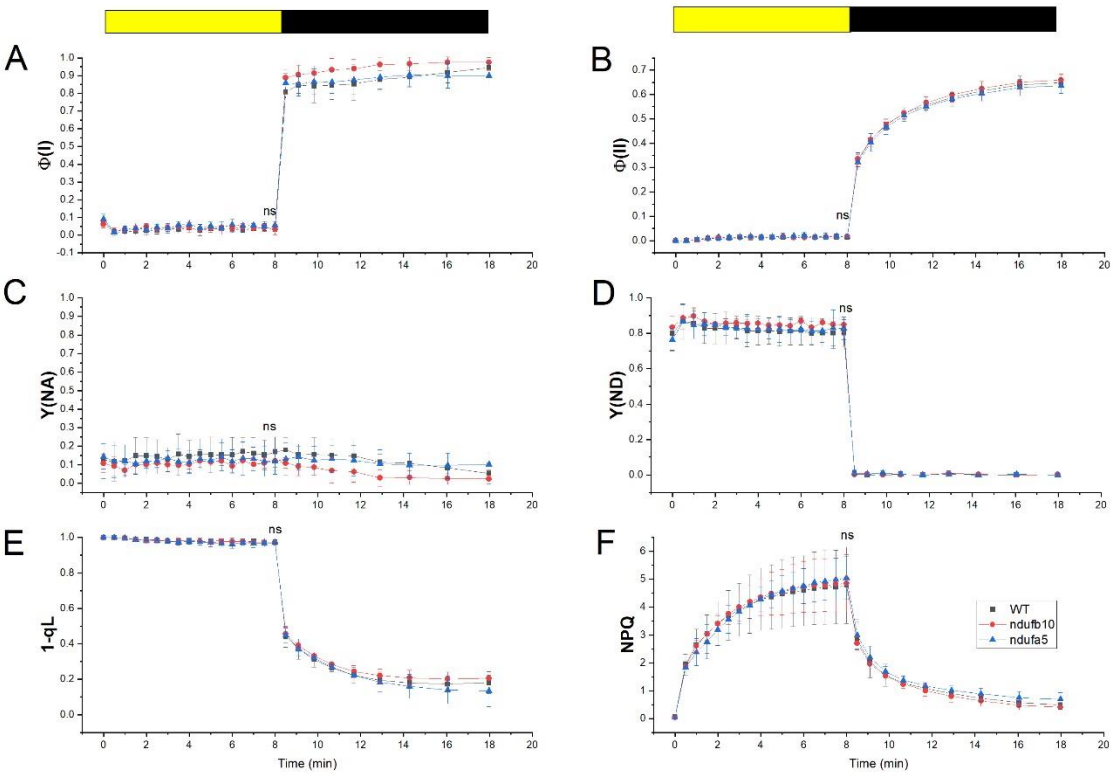

Supplemental Figure S6. Photosynthetic efficiency under saturating illumination. The yield of PSI (Φ(I), A), PSII (Φ(II), B). PSI acceptor side limitation (Y(NA), C), PSI donor side limitation (Y(ND), D). PQ redox state (1-qL; E) and non-photochemical quenching (NPQ; F) under 2000 µmol photons $m^{-2}s^{-1}$ of light intensity. WT, *ndufb10* and *ndufa5* KO are shown respectively with black square, red circle and cyan triangle. Yellow boxes above the panels represent actinic light on, instead black boxes represent actinic light off. Data are shown as average ± SD (n > 4). Statistical analysis was performed for the last point of illumination before light was switched off (one-way ANOVA, n > 4, $p < 0.01$; ns = not significant).

Supplemental Figure S7.

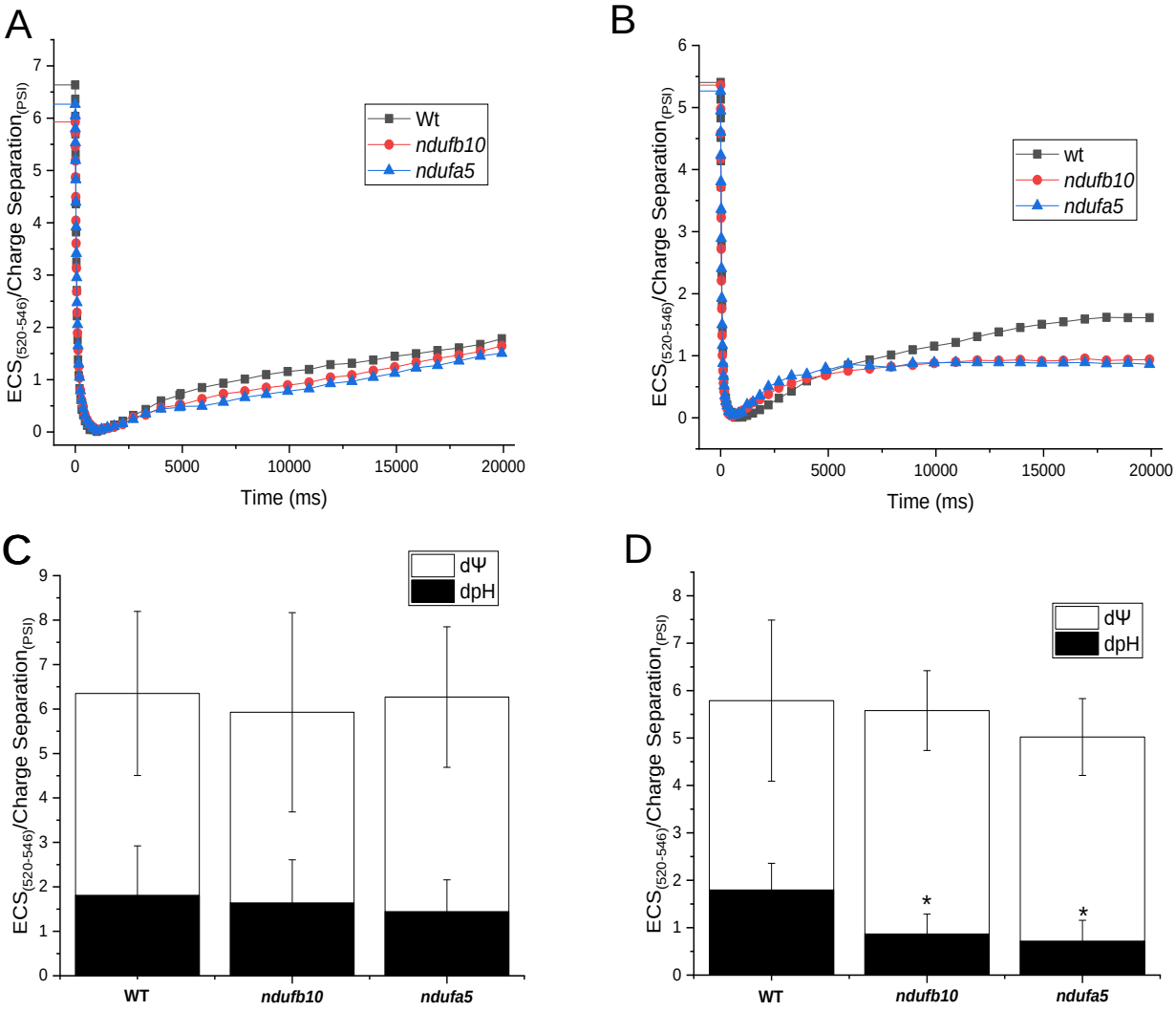

Supplemental Figure S7: Proton motive force composition before the steady state. A-B) Representative traces of the ECS (Electro-Chromic Shift) signal after the light is switch off after 60 s (A) and 120 s (B) of illumination (300 µmol photons m^{-2} s^{-1}). WT, *ndufb10* and *ndufa5* KO are shown respectively as black squares, red circles and blue triangles. C-D) pmf partitioning after 60 s (C) and 120 s (D) is represented with black columns for ΔpH component and white columns for the electrical potential (ΔΨ) Data are shown as average ± SD. For D asterisks indicate statistically significant differences (one-way ANOVA, $n > 5$, $p < 0.01$).

Supplemental Figure S8.

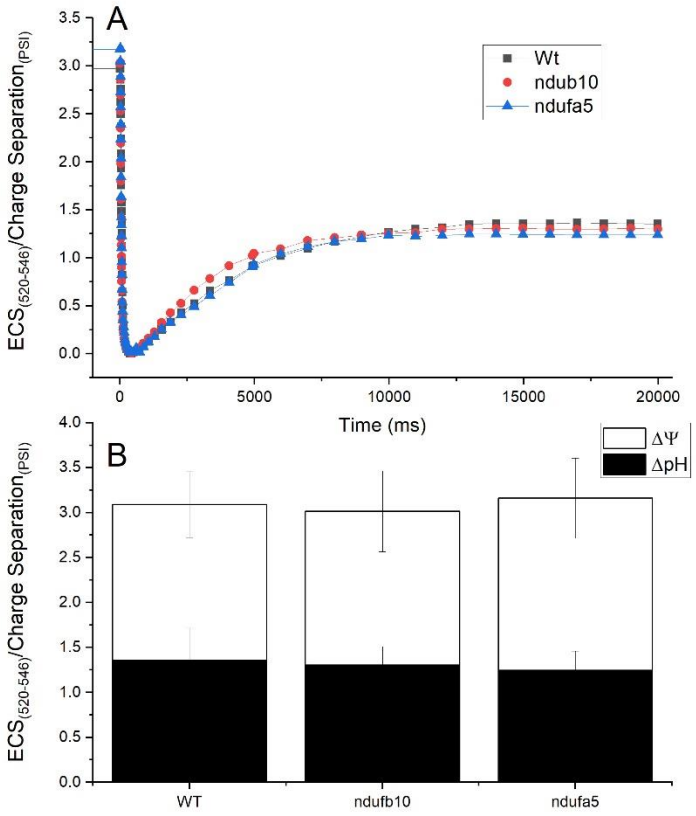

Supplemental Figure S8: Photosynthetic proton motive force at saturating illumination. Proton motive force (pmf) generated in thylakoids membranes assessed by ECS (Electro-Chromic Shift) signal in plants exposed for 300 seconds of illumination with saturating light (900 µmol m^{-2} s^{-1}). A) Representative tracks of the ECS signal after light is switch off. WT, *ndufb10* and *ndufa5* KO are shown respectively with black square, red circle and cyan triangle. B) Black columns are representative for the osmotic components (ΔpH) of pmf while white columns show the electrical potential (ΔΨ). Data are shown as average ± SD (n > 5).

Supplemental Figure S9.

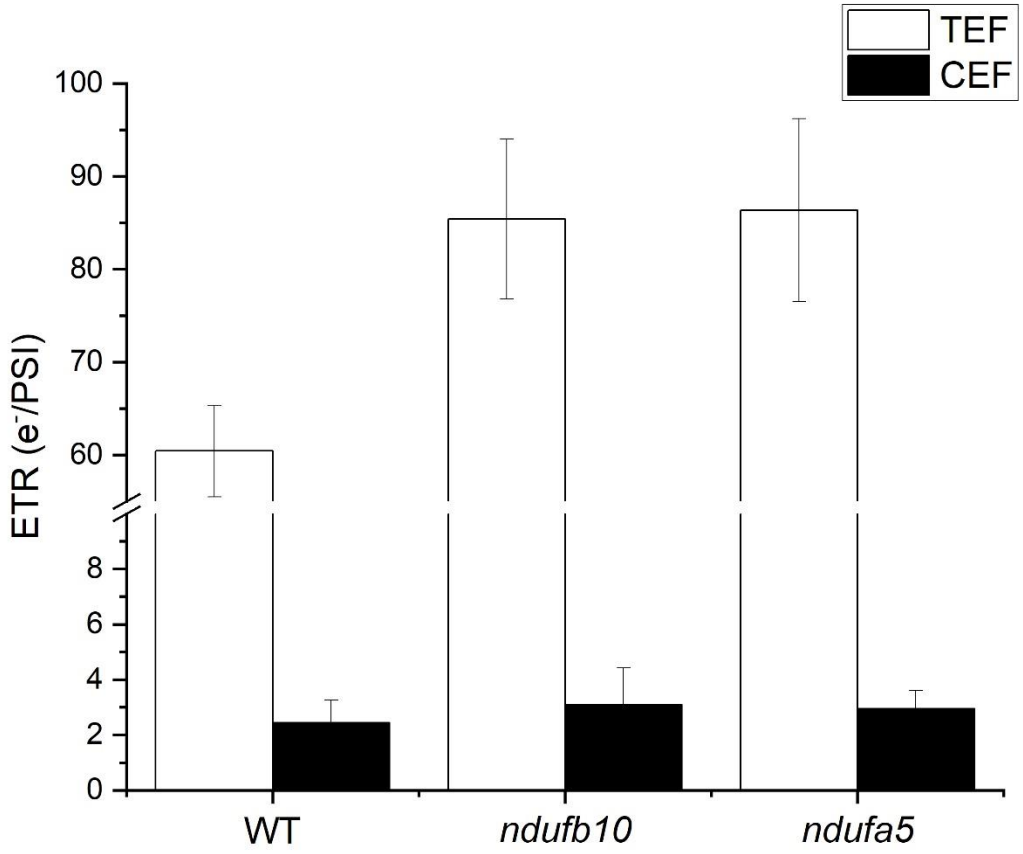

Supplemental Figure S9: Photosynthetic electron transfer (ETR) in *P. patens* plants. A) Total photosynthetic electron flow (TEF) and B) cyclic electron flow (CEF) measured in vivo in WT in *ndufb10* and *ndufa5* KO at 300 µmol photons $m^{-2}s^{-1}$ actinic light, calculated from electrochromic shift signal. Electron transport rate values are normalized to xenon-induced PSI turnovers. Data are shown as average ± SD (n > 4).

Supplemental Figure S10.

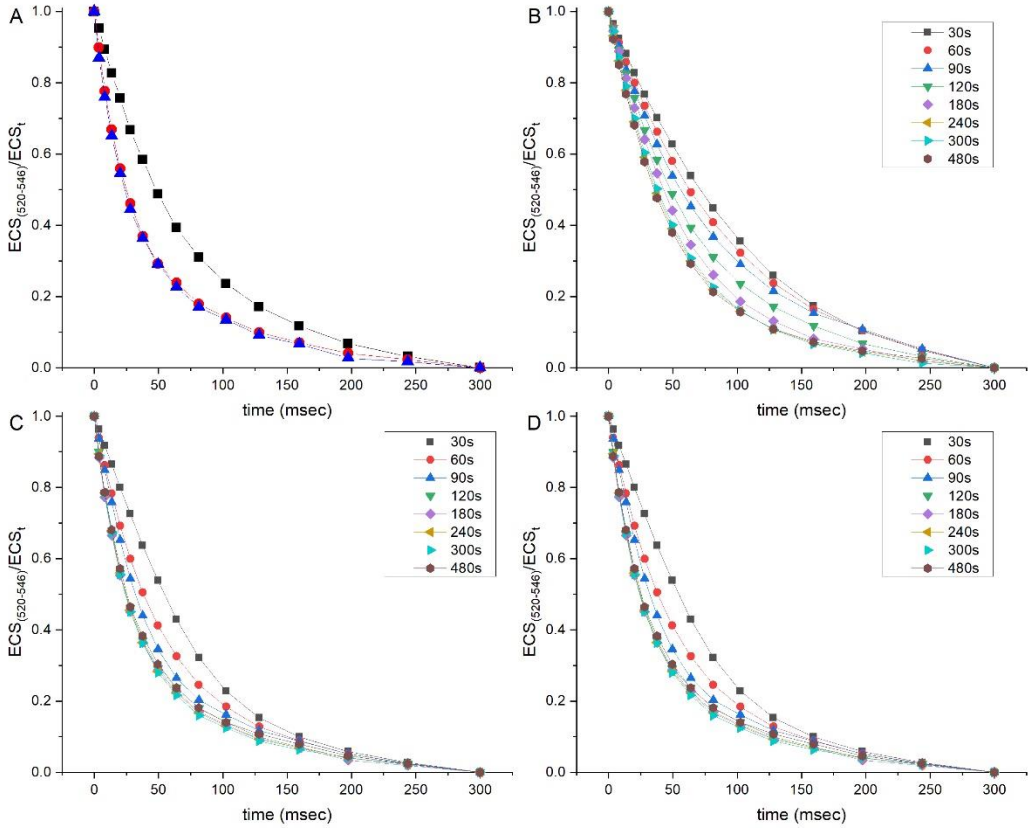

Supplemental Figure S10. ATPase activity assessed from ECS relaxation. A) Examples of ECS (Electro-Chromic Shift) relaxation kinetics after 120 seconds of illumination with sub-saturating light (300 µmol m^{-2} s^{-1}). WT, *ndufb10* and *ndufa5* KO are shown respectively as black squares, red circles and blue triangles. B-D) Examples of ECS relaxation traces for WT (B), *ndufb10* (C) and *ndufa5* (D) measured after illumination of different length. In every panel traces after 30, 60, 90, 120, 180, 240, 300 and 480 seconds are shown respectively as black squares, red circles, blue triangles, green triangles, magenta squares, ochre triangles, cyan triangles and carmine hexagons.

Supplemental Figure S11.

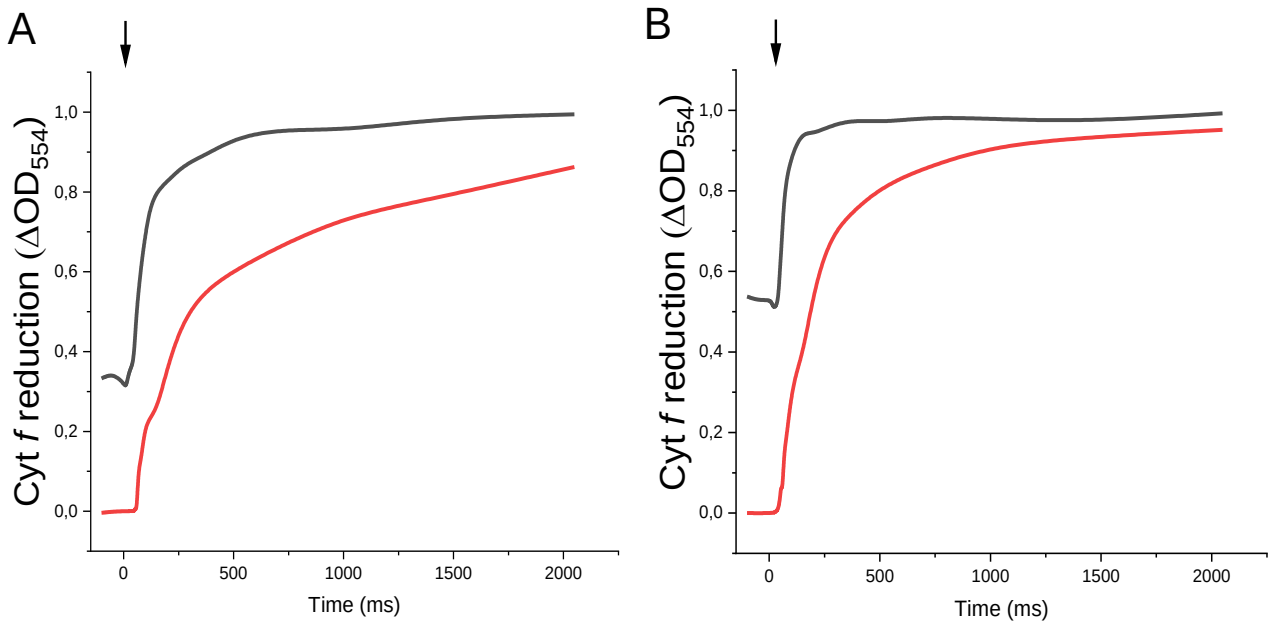

Supplemental Figure S11: Cyt *b6f* reduction state estimation. WT (A) and *ndufa5* (B) are here reported. Cyt *f* (cytochrome *f*) reduction showed in Figure 7 was measured by comparing the maximal signal obtained after 480 seconds under a saturating illumination (black line) with the signal obtained after treating the same sample by DCMU and DBMIB (red line). The traces here reported show the first 2000ms after light is switched off. The cyt *f* reduction rate was measured with a multiple exponential fitting of the complete cyt *f* reduction curve. All samples are normalized to the maximal signal. Arrows (t = 0): light off.

Supplemental Figure S12.

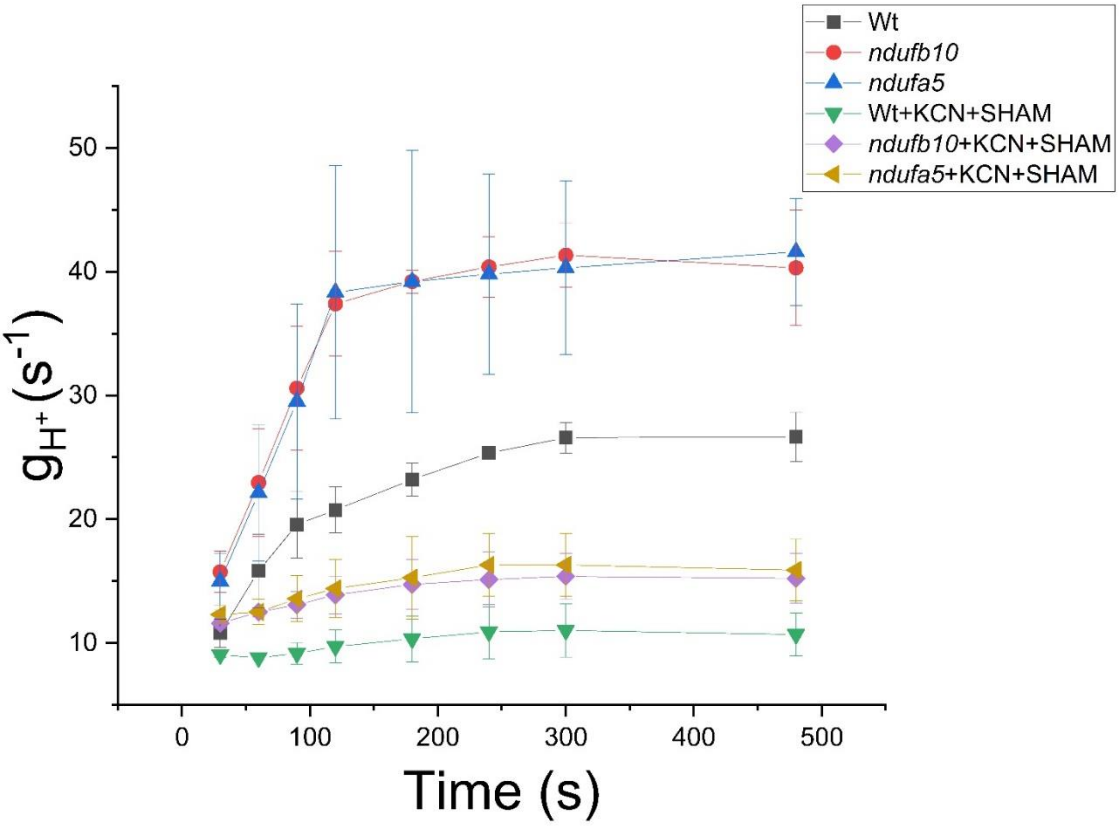

Supplemental Figure S12. Influence of respiration inhibition (KCN+SHAM) on proton conductivity (g_{H^+}) in WT and CI mutants. Proton conductivity (g_{H^+}) measured in control conditions and when respiration is fully inhibited in both WT and CI mutants with KCN 1mM and SHAM 8mM (as in Figure 4C). For control conditions WT, *ndufb10* and *ndufa5* KO are shown respectively with black squares, red circles and blue triangles. For the treatment with inhibitors WT, *ndufb10* and *ndufa5* KO are shown respectively with green triangles, magenta squares, ochre triangles. g_{H^+} was calculated after exposure to 30s, 60s, 90s, 120s, 180s, 240s, 300s and 480s of illumination (approx. 350 µmol photons $m^{-2}s^{-1}$) by fitting the first 300 ms of the ECS (Electro-Chromic Shift) decay curve with a first-order exponential decay kinetic and indicated as the inverse of the decay time constant (Avenson et al., 2005). Data are shown as average ± SD (n > 3).

Supplemental Figure S13.

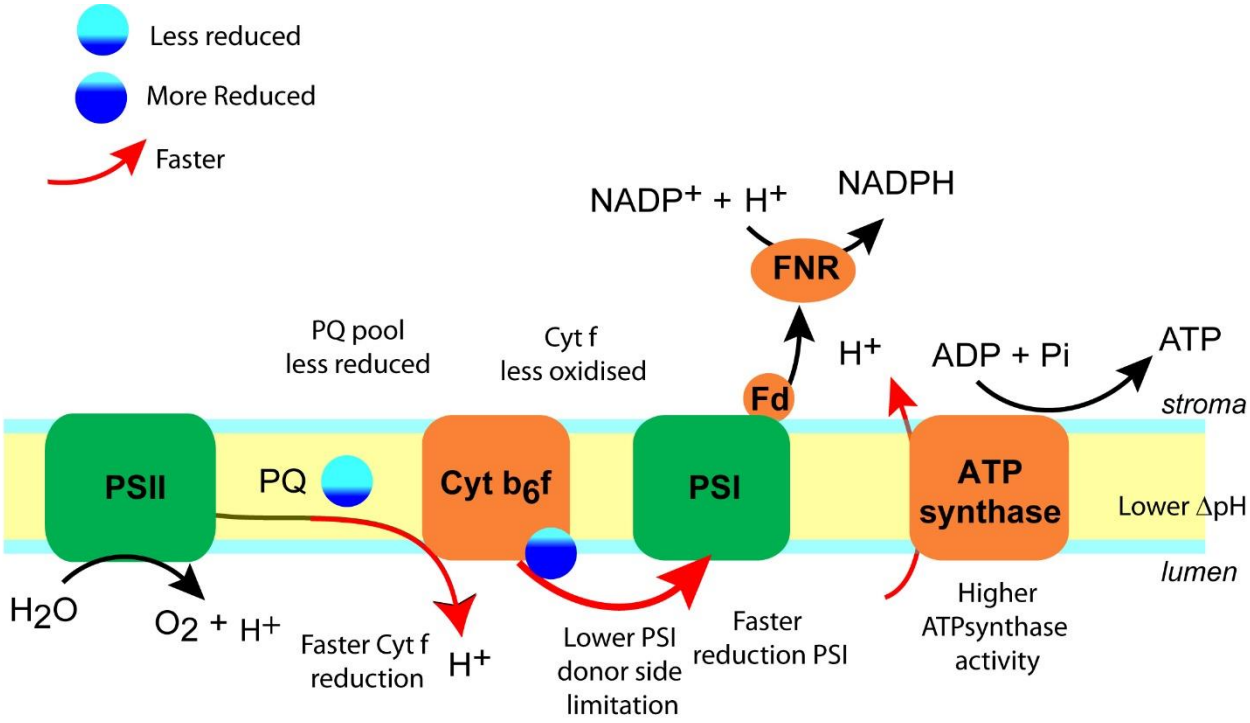

Supplemental Figure S13. Summary of photosynthetic electron transport alterations in CI depleted plants. Scheme of the main components of photosynthetic electron transport from water to NADP+ summarizing all differences observed in the mutants with respect to WT. PSI (II), Photosystem I (II); PQ, plastoquinone; Cyt, cytochrome; Fd, Ferredoxin; FNR, Ferredoxin NADP reductase.

Supplemental Table S1. Identification of conserved CI subunits in *P. patens*. Complex I subunits from *B. taurus*, *Y. lipolytica*, *C. reinhardtii* and *A. thaliana* were obtained from Salinas et al., 2014, Subrahmanian et al., 2016 and Klusch et al., 2020. Names of proteins are based on published papers and reviews (see references). *P. patens* nuclear homologous sequences were identified using BLAST facilities (https://blast.ncbi.nlm.nih.gov/Blast.cgi) with fungal, mammal, and plant protein and genic sequences against the *P. patens* genome (v3.3) (Lang et al., 2018; https://phytozome.jgi.doe.gov/pz/portal.html). Subunits encoded in the mitochondrial genome were identified from Terasawa et al., 2007. Name for the subunits in plants are reported only when they differ from animals or yeast. In red are indicated subunits that were confirmed by proteomic analyses (Mueller et al., 2014) In bold are indicated the subunits choose for inactivation of the complexes. a) Salinas et al., 2014; b) Subrahmanian et al., 2016; c) Terasawa et al., 2007; d)Klusch et al., 2020 e) Rak and Rustin, 2014; f) Barbieri et al., 2011; g) Klodmann et al., 2011, h) Mueller et al., 2014.

B. taurus	*Y. lipolytica*	*A. thaliana*	*C. reinhardtii*	*P. patens*	Ref.
Bacterial core					
ND1	ND1/ NU1M	AtMg00516, AtMg01120, AtMg01275	AAB93446, nd1	YP_539026	a, b, c, d
ND2	ND2/ NU2M	AtMg00285, AtMg01320	AAB93444, nd2	YP_539019	a, b, c, d
ND3	ND3/ NU3M	AtMg00990	AAQ55461, ND3	YP_539030	a, b, c, d
ND4	ND4/ NU4M	AtMg00580	AAB93441, nd4	YP_539018	a, b, c, d
ND4L	ND4L/ NULM	AtMg00650	AAO61142, nd4L	YP_539012	a, b, c, d
ND5	ND5/ NU5M	AtMg00060, AtMg00513, AtMg00665	AAB93442, nd5	YP_539016	a, b, c, d
ND6	ND6/ NU6M	AtMg00270	AAB93445, nd6	YP_539023	a, b, c, d
NDUFS1/ 75 kD	NUO78/ NUAM	At5g37510	XP_001692885, NUOS1	Pp3c1_34110, Pp3c1_34100, Pp3c1_34140, Pp3c19_19270	a, b, d, h
NDUFS2	NUO49/ NUCM	AtMg00510	XP_001697607, ND7	YP_539031	a, b, d, h
NDUFS3	NUO30.4	AtMg00070	XP_001690652, ND9	YP_539028	a, b, d, h
NDUFS7/ PSST	NUO19.3/ NUKM	At5g11770	XP_001700585, NUO10	Pp3c15_14890, Pp3c15_20620	a, b, d
NDUFS8/ TYKY	NUO21.3c/ NUIM	At1g16700, At1g79010	XP_001702368, NUO8	Pp3c9_8460, Pp3c15_4330	a, b, d
NDUFV1	51/ NUBM	At5g08530	XP_001702590, NUO6	Pp3c4_17990, Pp3c12_4050	a, b, d
NDUFV2	NUO24/ NUHM	At4g02580	XP_001698508, NUO5	Pp3c2_9810, Pp3c2_9813	a, b, d
Conserved supernumerary					
NDUFA1/ MWFE	NUO9.8/ NIMM	At3g08610	XP_001698399, NUOA1	Pp3c10_5690, Pp3c10_5720	a, b, d

NDUFA2/ B8	NUO10.5/ NI8M	At5g47890	XP_001695875, NUOB8	Pp3c20_8510	a, b, d
NDUFB3/ B12	NUO10.6/ NB2M	At2g02510, At1g14450	XP_001700920, NUOB12	Pp3c9_5250, Pp3c15_3960	a, b, d
NDUFA5/ B13	**NUO29.9/ NUFM**	**At5g52840**	**XP_001693453, NUOB13**	**Pp3c5_12290**	a, b, d, e
NDUFS6/ 13 kD	NUO18.4/ NUMM	At3g03070	XP_001703419, NUOS6	Pp3c24_2620	a, b, d
NDUFA6/ B14	NUO14.8/ NB4M	At3g12260	XP_001694042, NUOB14	Pp3c1_37620, Pp3c2_3180	a, b, d
NDUFA11/ B14.7	NUO21.3b/ NUJM	At2g42210	XP_001689829, TIM17	Pp3c5_22310, Pp3c6_9862	a, b, d
NDUFB11 /ESSS	NUO11.7/ NUWM	At3g57785, At2g42310	XP_001697702, NUO17	Pp3c3_16790	a, b, d
NDUFS5/ PFFD	NUO11.5/ NIPM	At3g62790, At2g47690	XP_001691060, NUOS5	Pp3c7_20680, Pp3c11_13470	a, b, d
NDUFB4/B15	NUO6.6/ NUVM	At2g31490	XP_001693191, NUOB4	Pp3c16_220, Pp3c25_300	a, b, d
DAP13/ B17.2	NUO13.4	At3g03100	XP_001699522	Pp3c16_5910	a, b, d
NDUFB7/ B18	NB8M	At2g02050	XP_001698082, NUOB18	Pp3c10_11190, Pp3c14_25130	a, b
NDUFA12/ B16.6	NUO14/ NB6M	At1g04630, At2g33220	XP_001701450, NUOB16	Pp3c5_4240, Pp3c16_2570	a, b, d
DAP13/ B17.2	NUO13.4/ N7BM	At3g03100	XP_001699522, NUO13	Pp3c16_5910	a, b
NDUFB7/ B18	NB8M	At2g02050	XP_001698082, NUOB18	Pp3c10_11190, Pp3c14_25130	a, b, d
NDUFS4/ AQDQ	NUO21/ NUYM	At5g67590	XP_001695601, NUOS4	Pp3c8_17050, Pp3c12_14210, Pp3c24_19370	a, b, d
NDUFA8/ PGIV	NUO20.8/ NUPM	At5g18800, At3g06310	XP_001700114, NUOA8	Pp3c3_33480, Pp3c4_6220, Pp3c10_17050	a, b, d
NDUFB9/ B22	NI2M	At4g34700	XP_001698797, NUOB22	Pp3c6_19130	a, b, d
NDUFB10/ PDSW	**NUO12.3/ NIDM**	**At1g49140, At3g18410**	**XP_001694041, NUOB10**	**Pp3c9_26150**	a, b, d, f
NDUFA9/ 39 kD	NUO40/ NUEM	At2g20360	XP_001702653, NUOA9	Pp3c1_35920, Pp3c14_9070	a, b, d
NDUFB8/ ASHI	NUO20.1/ NIAM	At5g47570	XP_001700273, TEF29	Pp3c20_8820	a, b, d
NDUFB2/AGGG	NCU01436	At1g76200	–	Pp3c18_1920, Pp3c21_21340	a, b, d
NDUFB1/ MNLL	NUO20.9/ NUXM	At4g16450	XP_001696533, NUO21	Pp3c6_28950	a, b, d, h
NDUFC2/ B14.5B	NUO10.4	At4g20150 (NDU9)	XP_001693474, NUOP1	Pp3c1_24730, Pp3c14_13800	a, b, d
NDUFC1/ KFYI	NCU08300	At4g00585	XP_001697243	Pp3c7_13700	a, b, d
NDUFA3/ B9	NUO9.5/ NI9M	At2g46540	XP_001692978	Pp3c23_12490	a, b, d

NDUFAB1/ ACPM	SDAP	At1g65290, At2g44620	XP_001699275, ACP1	Pp3c13_14790, Pp3c20_7570, Pp3c23_19250, Pp3c24_6630	a, b, d
NDUFA7	NCU08930	At5g08060	XP_001703194	Pp3c16_5680	a, b, d
NDUFA4/ MLRQ	NCU02016	At3g29970	–	Pp3c3_14700, Pp3c4_20270, Pp3c26_5980	a, b
NDUFA10	–	At1g72040	–	Pp3c12_15090	a, b
Plant specific					
–	–	At5g63510 (CAL1), At1g19580 (CA1), At3g48680 (CAL2), At1g47260 (CA2), At5g66510 (CA3)	XP_001703237, XP_001701594, XP_001696746 (γ-carbonic anhydrase)	Pp3c4_16870, Pp3c7_19540, Pp3c7_4200, Pp3c11_22520, Pp3c1_7500,	a, b, d, g, h
–	–	At2g28430	–	Pp3c7_7440	a, b, g
–	–	At5g14105 (P3), At1g67350 (P1), At1g68680, At2g27730 (P2) (membrane arm subunits)	–	Pp3c1_22500, Pp3c1_33450, Pp3c3_5450, Pp3c11_6600, Pp3c14_2790,	a, b, g, h
–	–	At3g07480 (Ferredoxin)	XP_001699817, NUOP3,	Pp3c2_31000, Pp3c9_680	a, b, d

Supplemental Table S2. Capacities of the cytochrome and the AOX pathways in WT and *ndufb10* and *ndufa5* plants. The cyt pathway capacity is defined as O_2 uptake in the presence of SHAM that was sensitive to KCN. The AOX pathway capacity is defined as the O_2 uptake in the presence of KCN that was sensitive to SHAM. Calculations were made from data in figure 4 and respiration activity in plants treated with SHAM only, also reported here. Data are shown as average ± SD (n > 4).

$nmolO_2/(mg_{Chl}*min)$	WT	*ndufb10*	*ndufa5*
Cyt capacity	52.9 ± 8.1	52.2 ± 8.4	54.4 ± 7.4
AOX capacity	36.0 ± 9.7	73.4 ± 6.6	72.4 ± 7.4
+ 8 mM SHAM	74.3 ± 7.6	73.1 ± 8.0	75.2 ± 7.0

Supplemental Table S3: Primers employed in this work

Gene	Primer Name	Sequence	Use
Ndufb10	Ndufb10-p1	GTTTAAACGGCCCTAATGACATAAGTCCC	KO isolation
	Ndufb10-p2	CTCGAGGTGGATGAATGATGCTGGTG	KO isolation
	Ndufb10-p3	ATCGATCAAGTCGAGAAGGCGAAGATC	KO isolation
	Ndufb10-p4	TTAATTAAGATGGCGTCGAGTTCCTTCATC	KO isolation
	Ndufb10-p5	GGATCCACAATCAGGAATTA	KO screening
	Ndufb10-p6	ACCAAAGCAGTCCTGAAC	KO screening
	Ndufb10-RTf	GTTCAACAGCGACTACCCTA	RT-PCR
	Ndufb10-RTr	GAAACCCTTGTTCTGAAATG	RT-PCR
Ndufa5	Ndufa5-p1	CCTAGGCAATTCAGTATCCCTTACGC	KO isolation
	Ndufa5-p2	CTCGAGGGTCTGGTTTCCAACAATAA	KO isolation
	Ndufa5-p3	GTTAACGATGTTGACATGCACAGAAG	KO isolation
	Ndufa5-p4	TTAATTAAGACAACTAGGAACCATCCAA	KO isolation
	Ndufa5-p5	ATCAAACCCTGTACACCAAC	KO screening
	Ndufa5-p6	TGCAACTCATCTGTCCAATA	KO screening
	Ndufa5-RTf	TGCTTCATCATGTTTTTGAG	RT-PCR
	Ndufa5-RTr	AGAGCCAGATCAACAAGAAA	RT-PCR
Hygromycin resistance cassette	HNZ Up rev	TGCGCAACTGTTGGGAAG	KO screening
	HN Down for	CCGCTGAAATCACCAGTCTC	KO screening
Actin	Actin2f	GCGAAGAGCGAGTATGACGAG	KO screening, RT-PCR
	Actin2r	AGCCACGAATCTAACTTGTGATG	KO screening, RT-PCR

Bibliography

Avenson, T.J., Cruz, J.A., Kanazawa, A., Kramer, D.M., 2005. Regulating the proton budget of higher plant photosynthesis. Proc. Natl. Acad. Sci. U. S. A. 102, 9709–13. https://doi.org/10.1073/pnas.0503952102

Barbieri, M.R., Larosa, V., Nouet, C., Subrahmanian, N., Remacle, C., Hamel, P.P., 2011. A forward genetic screen identifies mutants deficient for mitochondrial complex I assembly in Chlamydomonas reinhardtii. Genetics 188, 349–58. https://doi.org/10.1534/genetics.111.128827

Klodmann, J., Senkler, M., Rode, C., Braun, H.-P., 2011. Defining the protein complex proteome of plant mitochondria. Plant Physiol. 157, 587–598.

Klusch, N., Senkler, J., Yildiz, Ö., Kühlbrandt, W., Braun, H.-P., 2020. A ferredoxin bridge connects the two arms of plant mitochondrial complex I. bioRxiv 2020.11.23.393975. https://doi.org/10.1101/2020.11.23.393975

Lang, D., Ullrich, K.K., Murat, F., Fuchs, J., Jenkins, J., Haas, F.B., Piednoel, M., Gundlach, H., Van Bel, M., Meyberg, R., Vives, C., Morata, J., Symeonidi, A., Hiss, M., Muchero, W., Kamisugi, Y., Saleh, O., Blanc, G., Decker, E.L., van Gessel, N., Grimwood, J., Hayes, R.D., Graham, S.W., Gunter, L.E., McDaniel, S.F., Hoernstein, S.N.W., Larsson, A., Li, F.-W., Perroud, P.-F., Phillips, J., Ranjan, P., Rokshar, D.S., Rothfels, C.J., Schneider, L., Shu, S., Stevenson, D.W., Thümmler, F., Tillich, M., Villarreal Aguilar, J.C., Widiez, T., Wong, G.K.-S., Wymore, A., Zhang, Y., Zimmer, A.D., Quatrano, R.S., Mayer, K.F.X., Goodstein, D., Casacuberta, J.M., Vandepoele, K., Reski, R., Cuming, A.C., Tuskan, G.A., Maumus, F., Salse, J., Schmutz, J., Rensing, S.A., 2018. The Physcomitrella patens chromosome-scale assembly reveals moss genome structure and evolution. Plant J. 93, 515–533. https://doi.org/10.1111/tpj.13801

Mueller, S.J., Lang, D., Hoernstein, S.N.W., Lang, E.G.E., Schuessele, C., Schmidt, A., Fluck, M., Leisibach, D., Niegl, C., Zimmer, A.D., Schlosser, A., Reski, R., 2014. Quantitative Analysis of the Mitochondrial and Plastid Proteomes of the Moss Physcomitrella patens Reveals Protein Macrocompartmentation and Microcompartmentation. Plant Physiol. 164, 2081–2095. https://doi.org/10.1104/pp.114.235754

Rak, M., Rustin, P., 2014. Supernumerary subunits NDUFA3, NDUFA5 and NDUFA12 are required for the formation of the extramembrane arm of human mitochondrial complex I. FEBS Lett. 588, 1832–1838. https://doi.org/10.1016/j.febslet.2014.03.046

Salinas, T., Larosa, V., Cardol, P., Maréchal-Drouard, L., Remacle, C., 2014. Respiratory-deficient mutants of the unicellular green alga Chlamydomonas: a review. Biochimie 100, 207–18. https://doi.org/10.1016/j.biochi.2013.10.006

Subrahmanian, N., Remacle, C., Hamel, P.P., 2016. Plant mitochondrial Complex I composition and assembly: A review. Biochim. Biophys. Acta - Bioenerg. 1857, 1001–1014. https://doi.org/10.1016/j.bbabio.2016.01.009

Terasawa, K., Odahara, M., Kabeya, Y., Kikugawa, T., Sekine, Y., Fujiwara, M., Sato, N., 2007. The mitochondrial genome of the moss Physcomitrella patens sheds new light on mitochondrial evolution in land plants. Mol. Biol. Evol. 24, 699–709. https://doi.org/10.1093/molbev/msl198